

Optical Design of PICO, a Concept for a Space Mission to Probe Inflation and Cosmic Origins

Karl Young^{a†}, Marcelo Alvarez^b, Nicholas Battaglia^c, Jamie Bock^d, Jullian Borrill^e, David Chuss^f, Brendan Crill^g, Jacques Delabrouille^h, Mark Devlinⁱ, Laura Fissel^j, Raphael Flauger^k, Daniel Green^l, Kris Gorksi^g, Shaul Hanany^a, Richard Hills^m, Johannes Hubmayrⁿ, Bradley Johnson^o, Bill Jones^c, Lloyd Knox^p, Al Kogut^q, Charles Lawrence^g, Tomotake Matsumura^r, Jim McGuire^g, Jeff McMahon^s, Roger O'Brient^g, Clem Pryke^a, Xin Zhi Tan^a, Amy Trangsud^g, Qi Wen^a, and Gianfranco de Zotti^t

^aUniversity of Minnesota, USA

^bUniversity of California Berkeley, USA

^dCalifornia Institute of Technology, USA

^eLawrence Berkeley National Laboratory, USA

^fVillanova University, USA

^gJet Propulsion Laboratory, California Institute of Technology, USA

^hLaboratoire AstroParticule et Cosmologie adn CEA/DAP, France

ⁱUniversity of Pennsylvania, USA

^jNRAO, USA

^kUniversity of California, USA

^lUniversity of Toronto, Canada

^mCavendish Laboratory, University of Cambridge, UK

ⁿNIST, USA

^oColumbia University, USA

^cPrinceton University, USA

^pUniversity of California Davis, USA

^qGoddard Space Flight Center, USA

^rKalvi IPMU, University of Tokyo, Japan

^sUniversity of Michigan, USA

^tOsservatorio Astronomico di Padova, Italy

ABSTRACT

Abstract Submitted Nov. 2017, needs polishing.

The Probe of Inflation and Cosmic Origins (PICO) is a probe-class mission concept currently under study by NASA. PICO will probe the physics of the Big Bang and the energy scale of inflation, constrain the sum of neutrino masses, measure the growth of structure in the universe, and constrain its reionization history by making full sky maps of the cosmic microwave background with sensitivity 70 times higher than the Planck space mission. With bands at 21-799 GHz and arcmin resolution at the highest frequencies, PICO will make polarization maps of galactic synchrotron and dust emission to observe the role of Galactic magnetic fields in galactic evolution and star formation. We describe the current state of the PICO instrument design. We will discuss the choice of optical system, present the design of the focal plane, and give the expected noise level.

Keywords: Cosmic microwave background, cosmology, mm-wave optics, polarimetry, instrument design, satellite, mission concept

[†]E-mail: kyoung@astro.umn.edu, Telephone: 1 612 626 9149

1. INTRODUCTION

Probe study language copied directly from Brian’s paper (May 6th). What level of repeat is useful? What is appropriate?

In astronomy and astrophysics, NASA currently flies small and medium Explorer missions (<\$250M), as well as multi-billion-dollar flagship observatories like JWST and WFIRST. There are a number of science opportunities that are beyond the scope of the Explorer program, but don’t require flagship-level funding. To explore these opportunities, NASA has funded studies of 10 ‘Probe’ class (\$400M-\$1B) mission concepts. The Probe of Inflation and Cosmic Origins (PICO) is one of these mission studies. Reports of these mission studies are due to NASA at the end of the 2018 and NASA’s plan is to forward the reports for consideration by the next Astronomy and Astrophysics Decadal panel. This paper comes part way through the PICO study, and describes a snapshot of the instrument design at this time in the study.

Astrophysical observations in the millimeter and sub-millimeter region of the electromagnetic spectrum contain a wealth of information about the formation, evolution, and current structure of the Universe. Large scale cosmological and fundamental physics information, such as evidence of inflation, the effect of the first stars and galaxies, constraints on neutrino masses, and limits on light particles beyond the standard model, is contained in the temperature and polarization anisotropies of the cosmic microwave background (CMB). Information about the role of magnetic fields in star formation and galactic evolution is obtainable by observing the polarized emission of Galactic dust, which traces magnetic fields, at high resolution. Targeting both of these regimes, PICO will survey the entire sky with unprecedented polarization sensitivity in 21 bands centered at 21–799 GHz. Details of these science targets and expected constraints from PICO are in a companion paper, Sutin et al.¹ In this paper we discuss the optical system, focal plane, and expected sensitivity of PICO.

2. SPACECRAFT AND MISSION

The PICO will conduct scientific observations for five years from the Earth-Sun L2 Lagrange point. The spacecraft design impacts the optical design and sensitivity in two primary ways; volume constraints limit the physical size of the telescope and optical component temperatures impact noise levels.

The maximum size of the spacecraft is limited by the launch vehicle, the Falcon 9, which carries payloads up to 4.6 m in diameter. This diameter limit sets the V-groove size which, along with the scan strategy, defines the ‘shadow cone’ in Figure 1. The shadow cone is the volume protected from solar illumination, and all optical components must remain within it. The shadow cone and inner V-grooves define an available volume for the telescope.

The temperatures of all optical elements are given in Figure 1. The optics box, secondary, and focal plane are actively cooled, details of the thermal system are given in Sutin et al.¹

3. OPTICAL SYSTEM

The PICO telescope is a 1.4 m modified Open Dragone. This choice was driven by a combination of science requirements and the physical limits discussed in Section 2. The science requirements are; a large diffraction limited field of view (DLFOV) sufficient to support $\mathcal{O}(10^4)$ detectors, arcminute resolution at 800 GHz, low instrumental polarization, and low sidelobe response. Additionally, the transition edge sensor bolometers baselined for PICO require a telecentric focal plane which is sufficiently flat that it can be tiled by 10 cm detector wafers without reduction in optical quality. These requirements suggest an off-axis Dragone system² similar to what has been used for *Planck*,³ various ground based systems such as ACT⁴ and SPT,⁵ and in the CORE⁶ and LiteBIRD⁷ designs.

The geometric parameters of the PICO optical system are given in Table 1 and the ray trace in Figure 2. The system is diffraction limited, Strehl greater than 0.8, at the center of the field of view for 799 GHz and has a DLFOV of 82.4 deg² at 155 GHz. Strehl of 0.8 contours for all pixel types are shown in Figure 2. The focal plane is telecentric to within 0.12° across the entire surface.

To arrive at the final design we modify an Open Dragone. We design the initial Open Dragone following Granet’s method.⁸ We find a solution which satisfies the volume constraints and has a large DLFOV. We force

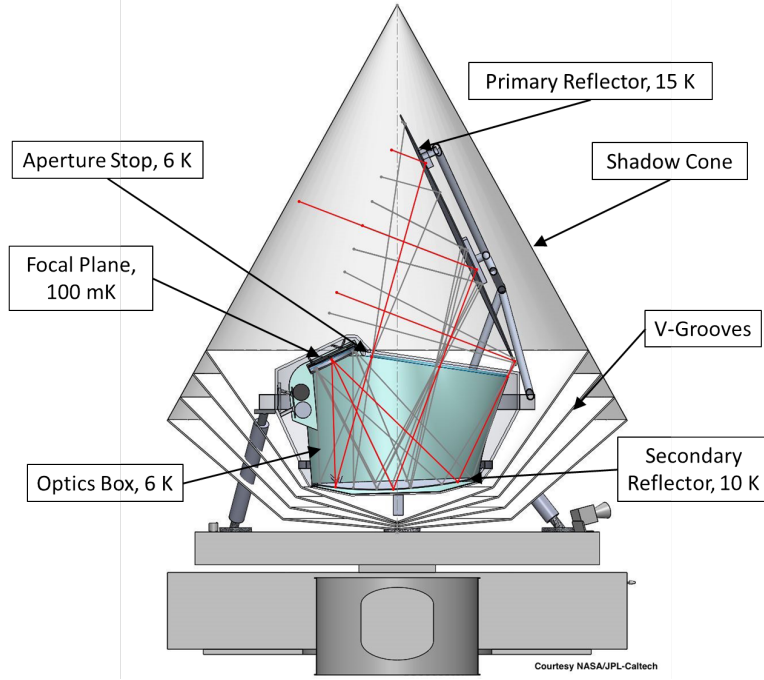


Figure 1. Mechanical design of the PICO satellite. Components relevant to this paper are labeled, for other details see Sutin et al.¹

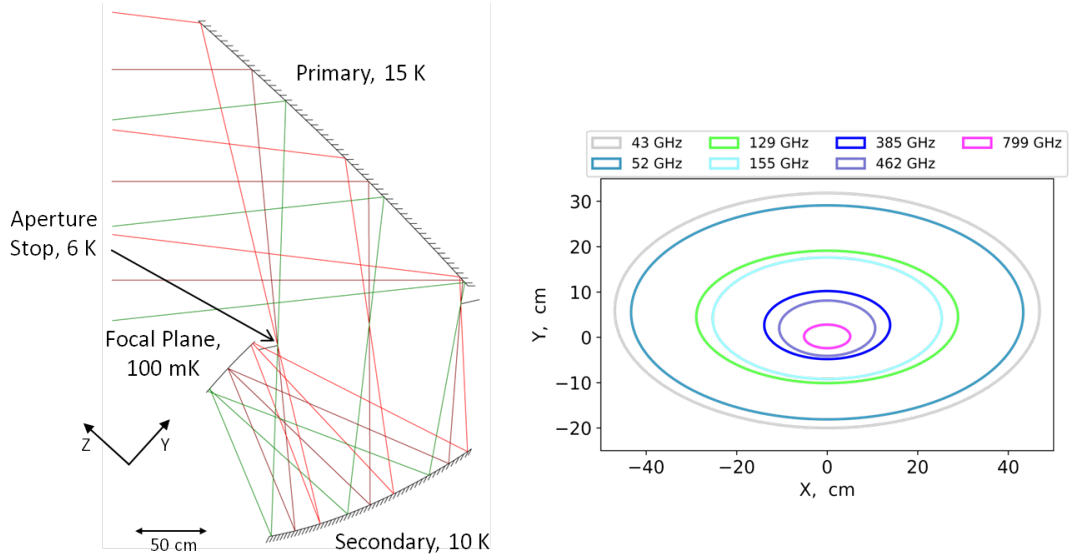


Figure 2. Raytrace (left) and Strehl = 0.8 contours (right) for the PICO optical design.

a circular aperture stop between the primary and secondary mirrors and numerically optimize its angle and position to obtain the best optical performance. We choose the stop diameter to provide an effective 1.4 m aperture on the primary for the center feed. Adding a stop in this way increases the size of the primary mirror, the primary is unevenly illuminated at various field angles, but reduces detector noise, see Section 5, and controls sidelobes. At this stage the system still meets the Dragone condition and is defined by the ‘Initial Open Dragone’ parameters in Table 1.

Table 1. Telescope geometric parameters

PICO optical system					Initial Open Dragone ^b	
	Primary	Secondary	Telescope parameters ^b		Fundamental design parameters	
Mirror size ^a (cm)	270 × 205	160 × 158	Aperture (cm)	140	Aperture (cm)	140
Radius of curvature (cm)	∞	136.6	Focal ratio, F	1.42	θ_0 (degrees)	90
Conic constant, k	0	-0.926	h (cm)	624.2	θ_e (degrees)	20
Normalization radius (cm)	524.8	194.1	α (deg)	74.2	θ_p (degrees)	140
4th Zernike Coefficient	2018.4	-61.1	β (deg)	62.3	L_m (cm)	240
9th Zernike Coefficient	-37.0	16.7	L_m (cm)	229.3	Derivative parameters	
10th Zernike Coefficient	-2919.8	-15.1	L_s (cm)	140.5		
11th Zernike Coefficient	-1292.7	22.3	Focal Plane		Focal ratio, F	1.42
12th Zernike Coefficient	120.6	-3.8			h (cm)	624.2
13th Zernike Coefficient	-74.5	4.9			α (deg)	38.6
19th Zernike Coefficient	-75.8	3.4			β (deg)	101.4
20th Zernike Coefficient	-398.9	6.3	Diameter (cm)	69 x 45	L_s (cm)	122.2
21st Zernike Coefficient	-319.5	23.3	Diameter (deg)	19 x 13	Primary, f (cm)	312.1
22nd Zernike Coefficient	-276.6	-8.5	Radius of curvature (cm)	455	Secondary, a (cm)	131
23rd Zernike Coefficient	-201.6	-3.2			Secondary, e	1.802
24th Zernike Coefficient	-127.4	-1.9				
25th Zernike Coefficient	-55.0	0.1				

^a The maximum physical size of the mirrors.

^b Telescope parameters follow the definitions in Granet 2001.⁸

Richard's final method used zernike polynomials similar to Jim's. Zemax defines offset Zernikes in a way CodeV does not, so the Zernike method only works in Zemax. I describe it below.

We pursued two methods to increase the DLFOV. The first follows a procedure by Richard Hills to numerically implement Dragone's corrections to eliminate coma.⁹ Dragone's correction calls for a distortion of the primary and secondary which goes as r^4 where $r = 0$ is at the chief ray impact point on each mirror. We implement this correction in Zemax by adding Zernike polynomials which are offset by $h = 624.2$ cm for the primary and 76.1 cm for the secondary. This places the origin of polynomials at the chief ray impact point for each mirror. All Zernike terms up to fourth order and the first fifth order term were allowed to vary. The optimization metric was minimization of the rms spot size at the center of the FOV, $\pm 2^\circ$ in Y, and $\pm 4^\circ$ in X with the center of the FOV most heavily weighted. To constrain the optimization, the X and Y effective focal lengths are held fixed as is the impact point of the chief ray on the focal plane.

This optimization using only Zernike polynomials increases the diffraction limited area by 15% at 21 GHz, by $2.4\times$ at 155 GHz, and by $10.5\times$ at 799 GHz. We improve the system further by allowing the focal plane radius of curvature to vary and rerunning the optimization. This gives a 50% increase in diffraction limited area at all frequencies over the Zernike polynomials alone. Finally, an approximately 4% additional gain in area can be achieved by adding Zernike terms up to sixth order, allowing the secondary to focal plane distance to vary, adding a weighted constraint on the effective focal length, and adding fields with low weight to the rms spot size metric at $\pm 7.5^\circ$ in Y and $+15^\circ$ in X, without these additional fields the corrections at the mirror edges are not well constrained.

The other method by Richard has the first step of converting the conics into an on axis XY polynomial representation. Then the same procedure is followed. It is less well behaved during optimization. This second Richard method is what I replicated in CodeV.

The second optimization uses CodeV and allows more of the geometric parameters of the system to vary. To adjust the mirror shapes, we add a low order, 4th and 9th-13th, Zernike polynomial correction to each conic surface. The Zernike polynomials are defined on the same coordinates as the base conics. We allow the focal plane curvature and focal plane to secondary distance L_s to vary. The primary-secondary distance L_m , primary offset h , and the primary and secondary rotation angles, α and β , are varied as well. The optimization metric is the rms spot size across the field of view, with additional weighted constraints requiring telecentricity and maintaining the x- and y-focal lengths. We also added Lagrange constraints to enforce beam clearances and

place an upper limit on overall system size. Once the optimization covered to an acceptable optical system, we added the higher order Zernike terms, 19th-25th, and refined the mirror shapes using the same metric and constraints. The current PICO design is from this optimization procedure.

Figure 3 shows that the optimization reduces the overall telescope volume, allowing it to fit more easily within the shadow cone, and increases the DLFOV. The DLFOV increases by $1.9\times$ at 21 GHz and by $4.6\times$ at 799 GHz. The most important gain in the DLFOV is at 129 and 155 GHz where it increased by $3.8\times$ and $4.3\times$, respectively. This added area allows us to add ‘C’ and ‘D’ pixels which are critical to meeting PICO’s cosmology and fundamental physics science goals, because they contain the bands most sensitive to the CMB. Being able to pack 100’s of ‘C’ and ‘D’ pixels into the focal plane is what allows PICO to reach unprecedented levels of CMB sensitivity.

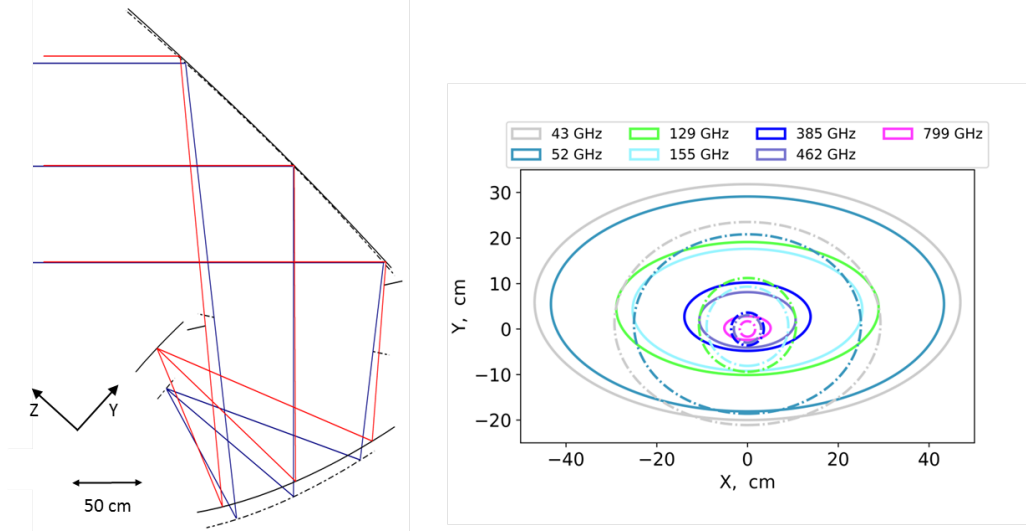


Figure 3. Comparison between optimized and unoptimized Open Dragones. The raytraces (left) are aligned at the chief ray impact point on the primary. The optimized system (red rays, solid mirrors) is smaller vertically and has a slightly flatter primary than the unoptimized version (blue rays, dash-dot mirrors). The overlaid Strehl = 0.8 contours (right) show the improvement at all frequencies in the optimized (solid lines) system over the unoptimized (dash-dot lines) system.

An additional benefit of the optimization is the concave focal plane. The Open Dragone’s focal surface is naturally curved, so matching this curvature reduces defocus and increases the DLFOV as well as increasing telecentricity. The unoptimized system is telecentric to within 2.5° while the optimized version is telecentric to within 0.12° . If the focal plane is too strongly curved tiling it with flat detector wafers would result in large defocus at the edges of these wafers. This is not the case for PICO. The focal plane radius of curvature, 4.55 m, results in a defocus of 0.1 mm for the edge of a 10 cm wafer.

We considered two additional Dragone systems; a Gregorian Dragone like that used for *Planck* and a Crossed Dragone similar to that planned for CORE or LiteBIRD. With half the diffraction limited focal plane area of the Open Dragone,⁶ the Gregorian Dragone is unable to support $\mathcal{O}(10^4)$ detectors, so was rejected. The Crossed Dragone has roughly $4\times$ the diffraction limited focal plane area of the Open, but it has well known issues with sidelobes as shown in Figure 4 and always has a larger F-number than the Open system. The larger F-number results in a larger telescope that fits poorly into the shadow cone. The largest Crossed Dragone that meets the PICO volume constraints has a 1.2 m aperture while the largest Open Dragone is 1.4 m. The large F-number of the Crossed system also increases the physical focal plane size, and therefore mass and cost, for a fixed number of pixels. These disadvantages, and the success of the optimized Open Dragone, led us to the final PICO optical system detailed in Table 1 and shown in Figure 2.

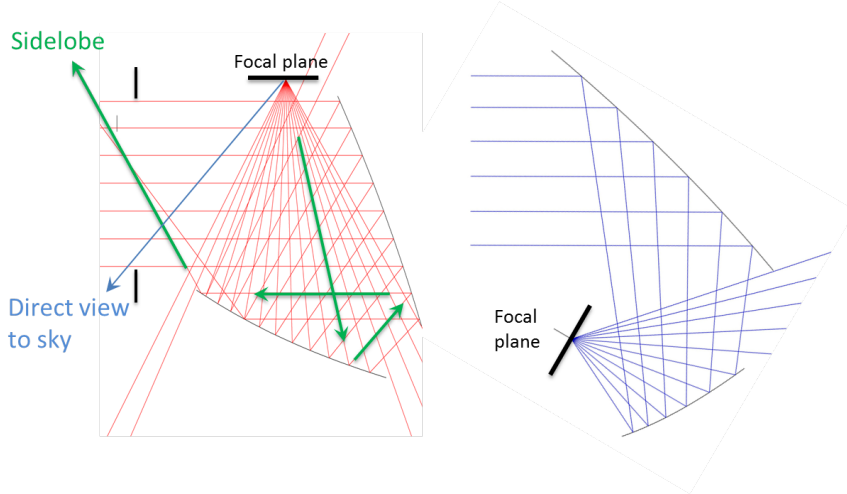


Figure 4. Comparison of sidelobes for typical example Crossed (left) and Open (right) Dragons. Rays are traced from the center of the focal plane toward the sky. For both systems spillover around the secondary is straightforward to mitigate with absorptive baffles. However, the sidelobe and direct sky view in the Crossed system require a long forebaffle or large F-number to mitigate, both of which are problematic in the PICO case.

4. FOCAL PLANE

Modern mm/sub-mm detectors are photon noise limited, so the primary way to increase sensitivity is to increase the number of detectors. The PICO focal plane has 12,996 detectors, $175\times$ the number flown on *Planck*. PICO achieves this by having a large DLFOV and using multichroic pixels (MCPs).¹⁰ The MCP architecture assumed for PICO has three bands per pixel with two single polarization transition edge sensor (TES) bolometers bolometers per band and therefore six bolometers total. We assume the MCPs are coupled to free space using lenslets,¹⁰ however the pixel size, number, and spacing is relatively agnostic to the coupling scheme, so the current layout would not change significantly if horn or phased array coupling was used instead.

We design PICO with 21 overlapping bands centered at 21–799 GHz and divided amongst nine pixel types, A–I; see Figure 5. These bands provide the broad frequency coverage needed to separate the CMB, Galactic dust, and various foregrounds using their differing spectra. The 25% fractional bandwidth is broader than the interband spacing, so the neighboring bands overlap and must be in separate pixels. For example, bands 1, 3, and 5 are in pixel A while bands 2, 4, and 6 are in pixel B. This complicates the pixel design and focal plane layout, but allows broader bands to increase total sensitivity.

The exceptions to this MCP architecture are the highest three bands. These three bands are above the superconducting band gap of niobium, so the niobium transmission lines and filters used in MCPs are unsuitable. Instead we will use polarization sensitive, feedhorn coupled bolometers at these frequencies, similar to the *Planck*¹¹ or Herschel SPIRE¹² detectors.

The PICO focal plane is designed to take maximum advantage of the large field of view. The optical quality peaks at the focal plane center and falls off with radius as shown in Figure 2. This pattern dictates the layout shown in Figure 6. The highest frequency pixels are centered on the focal plane and low frequency pixels are arranged around the edge. The maximum radial distance for a given pixel is the point where the Strehl ratio for the upper edge of the highest frequency band within that pixel equals 0.8. Interior to these contours, the ellipses in Figure 6, the Strehl ratio increases ensuring pixels are diffraction limited.

Optimizing the pixel size is a balance between the total number of pixels, N_{px} , and the efficiency with which they couple to the telescope. Smaller pixels pack more densely on the focal plane, $N_{px} \propto 1/D_{px}^2$, but over illuminate the stop which reduces optical efficiency and adds optical load. We choose a pixel diameter of $2.1F\lambda_{mid}$, where λ_{mid} refers to the center band of each pixel. This gives an edge taper, T_e , on the stop of 10 dB for the center band. Due to the multichroic nature of the pixels T_e varies with band, details in Section 5. We

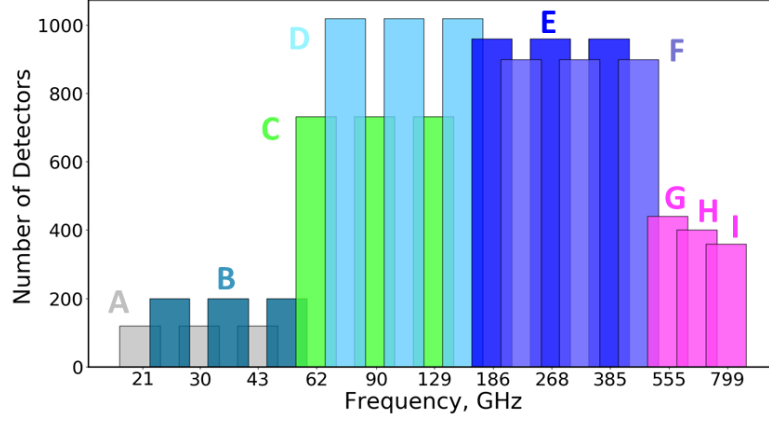


Figure 5. Frequency coverage of the PICO bands. Each color (excluding magenta) denotes a different MCP, labeled A-F. The bar height indicates the number of detectors per band. Width gives the bandwidth, all are top-hats with 25% fractional bandwidth; the x -axis is logarithmic. The three highest frequencies (magenta) are single color pixels G, H, I.

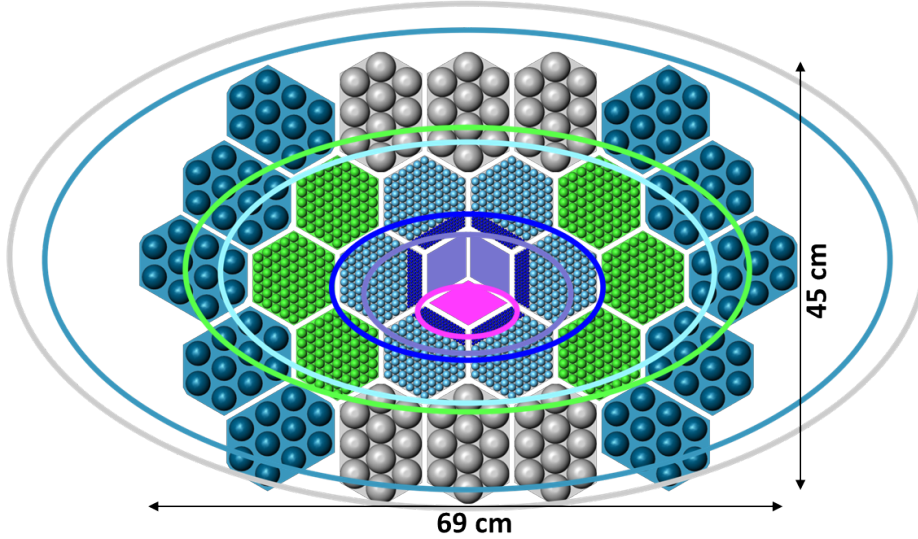


Figure 6. PICO focal plane layout with Strehl = 0.8 contours for each pixel type. The pixel and Strehl contour colors match the band colors, A-I, in Figure 5

hex-pack pixels onto 94 mm hexagonal wafers to minimize wasted space for the mid-frequency pixels. The three central wafers have the same 94 mm hexagon footprint but are split into 3 rhombi, shown in Figure 6, because the highest frequency magenta wafer will use different detector technology and will need to be fabricated separately.

The polarization sensitive bolometers in each MCP are oriented perpendicular to each other. Differencing the bolometers allows each pixel to measure Stokes Q or, if the pixel is rotated by 45° , Stokes U. We rotate neighboring pixels which scan over the same sky location by 45° , as shown in Figure 7. This layout reduces systematic errors by maximizing the number of Q,U pixel pairs which have almost identical optical paths and measure sky locations as close to simultaneously as possible.

Reading out 12,996 TES bolometers requires significant multiplexing. Time domain (TDM) and frequency domain (FDM) multiplexing were explored for PICO, tradeoff details are in Sutin et al.¹ The current PICO baseline is TDM, but the choice is not a driver for the focal plane layout or noise discussed in this paper.

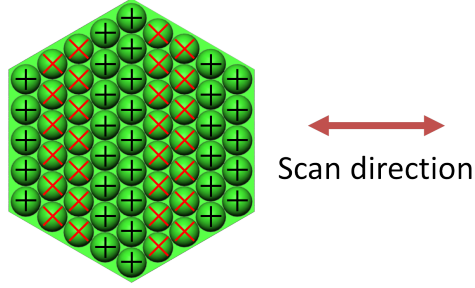


Figure 7. Layout of pixels sensitive to Stokes Q (black crosses) and Stokes U (red exes) for an example wafer.

5. INSTRUMENT NOISE

We develop an end to end white noise model of the PICO instrument to predict full mission sensitivity and provide a metric by which to evaluate optical, mechanical, and mission design tradeoffs. This model does not include 1/f noise or estimates of possible systematic effects. To construct the model we follow the standard process^{13,14} of estimating the optical load, calculating properties of the TES bolometers, calculating noise equivalent power (NEP) by source, combining all NEP terms to get detector noise, and finally combining all detectors to get full mission sensitivity. Each of these steps includes various assumptions and design decisions, which are discussed in this section. The assumptions are summarized in Table 2.

Table 2. Noise model assumptions, see text for details.

Throughput	single moded, λ^2
Fractional Bandwidth	25%
Mirror emissivity	$\epsilon = \epsilon_0 \sqrt{\nu/150 \text{ GHz}}$, $\epsilon_0 = 0.07\%$
Aperture stop emissivity	1
Low pass filter reflection loss	8%
Low pass filter absorption loss ^a	frequency dependent, 0.2%–2.8%
Bolometer absorption efficiency	70%
T_e , middle band in pixel (dB)	10
Bose noise fraction, ξ	1
Bolometer yield	100%
Bath temperature, T_o (mK)	100
TES critical temperature, T_c (mK)	187
Safety factor, P_{sat}/P_{abs}	2
Thermal power law index, n	2
Intrinsic SQUID noise (aW/ $\sqrt{\text{Hz}}$)	3
TES operating resistance, Ω	0.03
TES transition slope, α	100
TES loop gain	14
Mission length (years)	5
Observing efficiency	95%

^aAssumes separate metal mesh in polypropylene filters for each wafer.

5.1 Single bolometer noise

5.1.1 Model

The sources of optical load are the CMB, primary and secondary mirrors, aperture stop, and a low pass optical filter. These elements are shown schematically in Figure 8. The total load absorbed at the bolometer is the sum of the power emitted by each element reduced by the transmission efficiency of the elements between the

emitting surface and the bolometer. The absorbed power is,

$$P_{abs} = (((P_{CMB}\eta_{PRI} + P_{PRI})\eta_{stop} + P_{stop}(1 - \eta_{stop}))\eta_{SEC} + P_{SEC})\eta_{filter} + P_{filter})\eta_{bolo}, \quad (1)$$

where P_{elem} is the in band power emitted by a given element for a single polarization and η_{elem} is the efficiency of the element. Power emitted by the stop is a special case. We multiply P_{stop} by $(1 - \eta_{stop})$ because η_{stop} is spillover efficiency, the fraction of the throughput which passes through the stop, so $(1 - \eta_{stop})$ is the fraction of the throughput which views the stop.

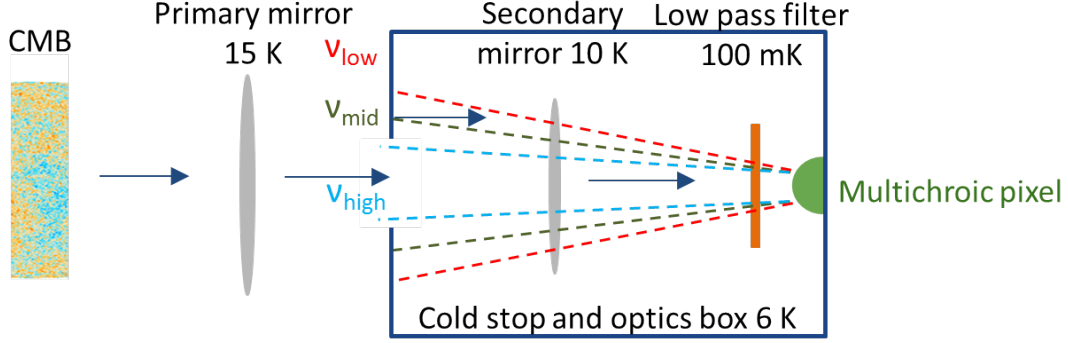


Figure 8. Schematic representation of the prediction of optical load. Power emitted by each element is modified by the efficiency of the following elements and added to the total expected load. The multichroic pixel illuminates the stop differently for each of the three bands.

For PICO, the CMB and stop dominate the optical loading as shown in Figure 9. The jumps in load between neighboring bands, seen in Figure 9 around 70 and 200 GHz, are due to η_{stop} changing with frequency which is a consequence of using MCPs. The MCP angular beam width is dependent on the wavelength and pixel diameter,¹³

$$\theta_{1/e^2} = \frac{2.95\lambda}{\pi D_{px}}. \quad (2)$$

The edge taper, T_e , of the middle frequency band in each pixel is chosen to be 10 dB. For the upper and lower bands T_e is calculated using Equation 2. This changing illumination of the stop is shown schematically by the dashed rays in Figure 8. For each MCP, A-H, T_e is 4.8, 10, and 20.7 dB for the lower, middle, and upper bands, respectively. These edge tapers correspond to η_{stop} of 0.68, 0.90, and 0.99. The changing η_{stop} has three main effects; uneven optical load between bands, varying NEP to noise equivalent temperature (NET) conversion between bands, and telescope beam size not scaling smoothly with λ .

We consider four noise sources per bolometer; photon, phonon, TES Johnson, and readout. Photon noise depends on the absorbed power,¹⁵

$$NEP_{\gamma}^2 = \int_{band} 2h\nu p_{\nu} d\nu + 2\xi \int_{band} p_{\nu}^2 d\nu, \quad (3)$$

where p_{ν} is the power spectral density for a single polarization absorbed at the bolometer and ξ is the fraction of correlated Bose photon noise. The extra factor of 2 in the Bose noise term is because we use single polarization bolometers. From P_{abs} we calculate the TES bolometer properties and phonon noise.¹⁶ The last noise term intrinsic to the bolometer is the TES Johnson noise. All noise sources in the cold and warm readout electronics are lumped under the readout term. The NEP for each noise source is shown in Figure 9.

5.1.2 Results

For PICO, photon noise dominates at all frequencies as shown in Figure 9. Bose noise is most significant at lower frequencies with $NEP_{Bose}/NEP_{Poisson} = 1.5$ in the lowest band. However, Poisson noise increases as $\sqrt{\nu}$,

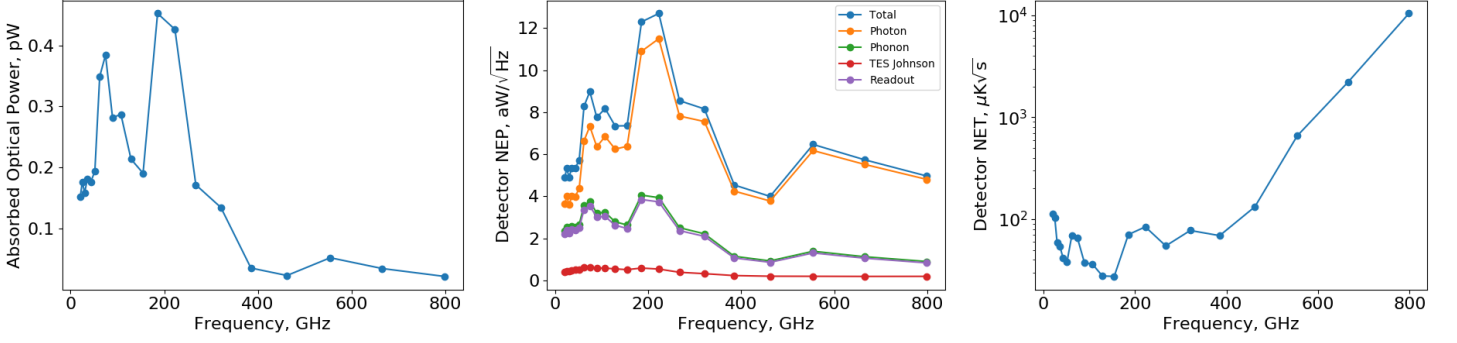


Figure 9. Left: Expected optical loads for single polarization PICO bolometers. Center: Breakdown of NEP across the PICO frequency range. Photon noise dominates even at the lowest frequencies. Right: Single detector NET, temperature sensitivity, across the PICO bands.

equalling Bose noise at 30 GHz and dominating at higher bands; $NEP_{Bose}/NEP_{Poisson} < 10\%$ at 321 GHz. Phonon noise is the second most significant source, $NEP_{phonon}/NEP_{photon}$ ranges from 65% at 21 GHz to 19% at 799 GHz.

For TDM readout phonon and readout noise are roughly equal, with TES Johnson noise being insignificant. We also modeled FDM readout. For FDM the TES Johnson noise is higher, 2/3 of the readout NEP, but the readout noise is lower. Comparing the combined Johnson and readout NEPs for TDM and FDM we find essentially identical performance with total noise differing by less than 3% across all bands. For either system we require a focal plane temperature, T_o , of 100 mK and a bolometer safety factor of 2 to remain photon noise dominated at the lowest bands.

The primary driver of noise levels is the optical load. The combination of the CMB and aperture stop make up the majority of the load in all bands. The load from the mirrors is greatest at 799 GHz where it is 90% of that from the CMB and stop. The CMB provides more than half the load in the middle and upper bands of the multi-chroic pixels, but the stop dominates the load in the lowest band of each pixel. Load from the stop in the lowest band of each pixel ranges from $1.2\times$ the CMB load at 21 GHz to a maximum of $4.7\times$ the CMB load at 223 GHz.

5.2 Combined array noise

Using single detector NEPs from Section 5.1 and the detector counts from Section 4 we calculate the combined NEP of the detector array for each band. Generally, combining detectors simply reduces noise by \sqrt{N} . The one exception is Bose photon noise. For the lowest band of each MCP the pixels oversample the PSF, pixel spacing is $0.4F\lambda$, resulting in correlated Bose noise between pixels. Accounting for this effect gives a 26% increase in the combined array NEP of the lowest band, 21 GHz, and only a 0.003% increase in the highest band, 799 GHz.

From the array NEP we convert to NET per band,

$$NET = \frac{NEP}{\sqrt{2}\eta_{opt} \int_{band} \left. \frac{dp_\nu}{dT} \right|_{T_{CMB}} d\nu}. \quad (4)$$

The η_{opt} term contributes to the ‘jumps’ in NET seen in Figure 9 since η_{opt} varies band to band.

All the above calculations have been for sensitivity to temperature and are given in Table 3. Assuming evenly weighted observations of the full sky and 5 years observing at 95% efficiency we calculate full mission map sensitivities in polarization; final column in Table 3. Combining all bands gives a total CMB map depth for the entire PICO mission of $0.62 \mu K_{CMB}$ -arcmin.

Table 3. PICO frequency channels and noise.

Pixel Type	Band GHz	FWHM arcmin	Bolometer NEP aW/\sqrt{Hz}	Bolometer NET $\mu\text{K}_{CMB}\sqrt{s}$	N_{bolo}	Array NET $\mu\text{K}_{CMB}\sqrt{s}$	Polarization map depth $\mu\text{K}_{CMB}\text{-arcmin}$
A	21	38.4	4.89	112.2	120	12.9	18.2
B	25	32.0	5.33	103.0	200	9.07	12.8
A	30	28.3	4.92	59.4	120	5.60	7.88
B	36	23.6	5.36	54.4	200	3.96	5.58
A	43	22.2	5.33	41.7	120	3.80	5.36
B	52	18.4	5.73	38.4	200	2.71	3.82
C	62	12.8	8.29	69.2	732	2.97	4.19
D	75	10.7	8.98	65.4	1020	2.34	3.29
C	90	9.5	7.76	37.7	732	1.41	1.99
D	108	7.9	8.18	36.2	1020	1.15	1.61
C	129	7.4	7.35	27.8	732	1.03	1.45
D	155	6.2	7.36	27.5	1020	0.86	1.21
E	186	4.3	12.30	70.8	960	2.39	3.36
F	223	3.6	12.70	84.2	900	2.89	4.07
E	268	3.2	8.55	54.8	960	1.77	2.49
F	321	2.6	8.16	77.6	900	2.59	3.64
E	385	2.5	4.54	69.1	960	2.23	3.14
F	462	2.1	4.00	132.6	900	4.42	6.22
G	555	1.5	6.47	657.8	440	31.4	44.1
H	666	1.3	5.74	2212	400	111	156
I	799	1.1	4.97	10430	360	550	774
Total					12996	0.44	0.62

6. CONCLUSIONS/SUMMARY

The PICO optical system is a simple two mirror Open Dragone which we numerically optimized to maximize the DLFOV. The addition of a cold aperture stop and cold mirrors minimize optical load and reduce noise. The focal plane takes advantage of the large DLFOV and MCP technology to implement 12996 polarization sensitive detectors in 21 bands from 21-799 GHz. When combining all bands, our instrument noise model predicts full mission polarization map depth of $0.62 \mu\text{K}_{CMB}\text{-arcmin}$.

7. ACKNOWLEDGEMENTS

This Probe mission concept study is funded by NASA grant xxxxxxxx. Gianfranco de Zotti acknowledges financial support from the ASI/University of Roma–Tor Vergata agreement n. 2016-24-H.0 for study activities of the Italian cosmology community. Jacques Delabrouille acknowledges financial support from PNCG for participating to the PICO study.

REFERENCES

- [1] Sutin, B. M., Alvarez, M., Battaglia, N., et al., “Pico - the probe of inflation and cosmic origins,” *Proc. SPIE* **10698** (2018).
- [2] Dragone, C., “Offset multireflector antennas with perfect pattern symmetry and polarization discrimination,” *Bell Labs Technical Journal* **57**(7), 2663–2684 (1978).
- [3] Fargant, G., Dubruel, D., Cornut, M., et al., “Very wide band telescope for Planck using optical and radio frequency techniques,” in [*UV, Optical, and IR Space Telescopes and Instruments*], Breckinridge, J. B. and Jakobsen, P., eds., *Proc. SPIE* **4013**, 69–79 (July 2000).
- [4] Swetz, D. S., Ade, P. A. R., Amiri, M., et al., “Overview of the Atacama Cosmology Telescope: Receiver, Instrumentation, and Telescope Systems,” *ApJS* **194**, 41 (June 2011).

- [5] Padin, S., Staniszewski, Z., Keisler, R., et al., “South Pole Telescope optics,” *Appl. Opt.* **47**, 4418–4428 (Aug. 2008).
- [6] de Bernardis, P., Ade, P. A. R., Baselmans, J. J. A., et al., “Exploring cosmic origins with CORE: The instrument,” *Journal of Cosmology and Astro-Particle Physics* **2018**, 015 (Apr. 2018).
- [7] Matsumura, T., Akiba, Y., Arnold, K., et al., “LiteBIRD: Mission Overview and Focal Plane Layout,” *Journal of Low Temperature Physics* **184**, 824–831 (Aug. 2016).
- [8] Granet, C., “Designing classical Dragonian offset dual-reflector antennas from combinations of prescribed geometric parameters,” *IEEE Antennas and Propagation Magazine* **43**, 100–107 (Dec. 2001).
- [9] Dragone, C., “First-order correction of aberrations in cassegrainian and gregorian antennas,” *IEEE Transactions on Antennas and Propagation* **31**, 764–775 (September 1983).
- [10] Suzuki, A., Arnold, K., Edwards, J., et al., “Multi-chroic dual-polarization bolometric detectors for studies of the cosmic microwave background,” *Journal of Low Temperature Physics* **176**, 650–656 (Sep 2014).
- [11] Lamarre, J. M., Puget, J. L., Ade, P. A. R., et al., “Planck pre-launch status: The HFI instrument, from specification to actual performance,” *A&A* **520**, A9 (Sept. 2010).
- [12] Griffin, M. J., Abergel, A., Abreu, A., et al., “The Herschel-SPIRE instrument and its in-flight performance,” *A&A* **518**, L3 (July 2010).
- [13] Suzuki, A., *Multichroic Bolometric Detector Architecture for Cosmic Microwave Background Polarimetry Experiments*, PhD thesis, University of California, Berkeley (Jan. 2013).
- [14] Aubin, F., *Detector Readout Electronics for EBEX: A Balloon-borne Cosmic Microwave Background Polarimeter*, PhD thesis, McGill University (2013).
- [15] Richards, P. L., “Bolometers for infrared and millimeter waves,” *Journal of Applied Physics* **76**, 1–24 (July 1994).
- [16] Mather, J. C., “Bolometer noise: nonequilibrium theory,” *Appl. Opt.* **21**, 1125–1129 (Mar. 1982).